Dual-Axis High-Data-Rate Atom Interferometer via Cold Ensemble Exchange

Akash V. Rakholia,[1,2] Hayden J. McGuinness,[1] and Grant W. Biedermann[1,2,*]

[1]*Sandia National Laboratories, Albuquerque, New Mexico 87185, USA*
[2]*Center for Quantum Information and Control (CQuIC), Department of Physics and Astronomy,*
University of New Mexico, Albuquerque, New Mexico 87131, USA
(Received 14 July 2014; published 24 November 2014)

We demonstrate a dual-axis accelerometer and gyroscope atom interferometer, which can form the building blocks of a six-axis inertial measurement unit. By recapturing the atoms after the interferometer sequence, we maintain a large atom number at high data rates of 50 to 100 measurements per second. Two cold ensembles are formed in trap zones located a few centimeters apart and are launched toward one another. During their ballistic trajectory, they are interrogated with a stimulated Raman sequence, detected, and recaptured in the opposing trap zone. We achieve sensitivities at $\mu g/\sqrt{\mathrm{Hz}}$ and $(\mu \mathrm{rad}/\mathrm{s})/\sqrt{\mathrm{Hz}}$ levels, making this a compelling prospect for expanding the use of atom interferometer inertial sensors beyond benign laboratory environments.

I. INTRODUCTION

Light-pulse atom interferometers (LPAIs) [1–3] demonstrate remarkably precise and stable measurements of acceleration and rotation. Numerous applications have been suggested, including gravimetry [4], seismology, inertial navigation [5–7], and near-surface force characterization [8]. However, such systems are typically designed for laboratory environments in pursuit of maximum sensitivity and, thus, are bulky and fragile, operating at the few-hertz rate. Lately, there has been great interest in adapting such systems to field use [9,10]. Adapting LPAI technology to this application space requires a compact sensor explicitly tailored for dynamic environments. Furthermore, inertial navigation requires a sensor capable of measuring both accelerations and rotations. Building on our previously reported high-data-rate accelerometer [11], we report a compact LPAI that is capable of simultaneous acceleration and rotation measurements and suitable for dynamic environments.

Our LPAI uses stimulated Raman transitions between hyperfine levels in a $\pi/2$-π-$\pi/2$ pulse sequence [12] to coherently separate, redirect, and recombine atomic wave packets from a cold atomic sample. The spatially dependent phase of the light field is imprinted on the atoms during each pulse. To first order, the resulting phase difference between the hyperfine levels is given by $\Delta\phi = \mathbf{k}_e \cdot (\mathbf{a} - 2\mathbf{v} \times \Omega)T^2$, where $\mathbf{k}_e$ is the effective Raman wave vector, T is the delay between pulses, and $\mathbf{v}$, $\mathbf{a}$, and Ω are the velocity, acceleration, and rotation of the atoms relative to the platform, respectively. Since $\mathbf{k}_e$ is typically locked to an atomic

transition, a precise determination of $\Delta\phi$ results in a precise measurement of acceleration and rotation.

The phase shift $\Delta\phi$ includes both acceleration and rotation contributions. If we consider a system of two independent interferometers [13] with phase shifts ϕ_a and ϕ_b, and opposing velocities $\mathbf{v}_a = -\mathbf{v}_b$, the sum and difference of the phases result in a term proportional to acceleration and rotation, respectively.

In a dynamic environment, a free-fall measurement such as this requires a short interrogation time [14] to curtail excursions of the ensemble. Because of the quadratic dependence of $\Delta\phi$ on T, a significant loss of sensitivity ensues. This can be compensated by using a large atom number and minimizing the dead time between measurements. We achieve both through recapture, recycling as many atoms as possible between shots [11]. Given the constraint of a small T, it is preferable to maximize velocity to maximize the rotation rate sensitivity. One method to achieve a large velocity while maintaining a high data rate is through the use of our ensemble exchange technique reported herein.

II. APPARATUS

Our ensemble exchange apparatus swaps cold atomic ensembles between two regions via launch and recapture. Two ensembles are simultaneously loaded in magneto-optical traps (MOTs) located a few centimeters apart. Through the use of conventional fountain launch techniques, the ensembles are launched towards each other at a velocity of a few meters per second. The interferometer takes place over several milliseconds during the ballistic transit between the two loading regions. At the end of the experiment, atoms are recaptured in the opposite trap from where they were launched. After a few milliseconds of recapture and loading, the cycle repeats. Thus, the atoms are "exchanged" between the trapping regions. Typically,

*Corresponding author.
gbieder@sandia.gov

the background-limited time it takes to load a MOT from vapor is on the order of a second. With recapture, the loading time is determined by the trap's time constant τ_{MOT}, which is typically on the order of several milliseconds [15].

We demonstrate this concept with a custom-built sensor head. The sensor head is designed around a rectangular quartz vacuum cell with inner dimensions of $20 \times 30 \times 60$ mm^3 and 3-mm-thick walls (Fig. 1). The use of high vacuum, as opposed to ultrahigh vacuum, significantly relaxes the vacuum requirements for the apparatus. Two magneto-optical traps of ^{87}Rb are loaded 36 mm apart at opposite ends of the cell from a background pressure of 2×10^{-7} Torr. The high vapor pressure is generated from a temperature-controlled source containing rubidium from a crushed ampoule. The high background vapor density allows for a fast short-term loading rate of 1×10^5 atoms/ms. This limits our coherence time to less than 100 ms, which is sufficiently high for our purposes. This vapor pressure represents a nearly optimal trade-off

between coherence time and MOT loading rate and occurs conveniently near the room-temperature vapor pressure of Rb.

The loading of two MOTs in close proximity is facilitated by small (approximately 16 mm length) quadrupole coils located 36 mm apart and a custom-designed opto-mechanical frame to support the necessary optics. The sensor head encloses a volume of approximately 5000 cm^3, excluding components of the high vacuum system. Because of the close proximity of the MOTs, the magnetic-field geometry changes based on the relative alignment of the quadrupole field polarities. Aligning the polarities in the same direction causes the magnetic-field gradient to vanish at points between the two traps, roughly one-quarter the distance between them. We align the polarities in a complementary opposing geometry to extend the high radial field gradient of 9 G/cm by a factor of 1.5. Furthermore, the optomechanical frame is machined out of the insulator G10 to diminish eddy currents and allow for fast magnetic-field switching, while maintaining a coefficient of thermal expansion similar to that of aluminum. The time constants for magnetic-field switching are 14 and 37 μs for bias and quadrupole coils, respectively. This ensures a sufficiently stable magnetic field during the interrogation time of our high-bandwidth experiment.

The apparatus uses optical access along four independent geometric planes to densely pack the required 19 optical beams and achieve a compact modular design. We find that a useful and compact simplification is to employ uncollimated cooling beams that diverge freely from the fiber at a half-angle of 5° [5]. For each MOT, we use 20 mW of cooling light locked at 12 MHz red of the $|F=2\rangle \rightarrow |F'=3\rangle$ cycling transition, corresponding to a total saturation parameter $s_0 = 15$. Additionally, 1 mW of repump light resonant with $|F=1\rangle \rightarrow |F'=2\rangle$ prevents accumulation of population in the dark state.

Figure 2 illustrates the launch and recapture process. Prior to the experiment, the quadrupole field is extinguished, and the inner and outer cooling beams are selectively detuned 2.2 MHz red and blue of the cooling frequency, respectively. This results in optical molasses in a moving frame at 2.5 m/s towards the center of the cell for both ensembles. The interferometer takes place as the atoms travel ballistically to the other side of the cell over 14 ms. To facilitate loading for the next shot, at the end of the experiment the traps are turned on and atoms are recaptured in the opposite trap. The characteristic capture time is given by $\tau_{MOT} = 2\hbar k/(\mu' A)$, where A is the magnetic-field gradient, and μ' is the effective magnetic moment of the transition used [15]. With our typical radial field gradient of 9 G/cm, we have $\tau_{MOT} = 2.0$ ms. Following recapture, atoms are launched again for the next shot of the experiment.
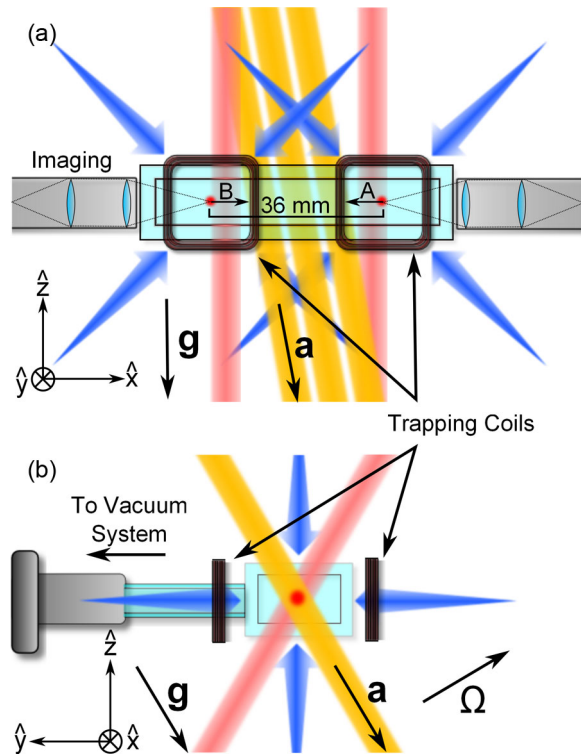

FIG. 1. Diagram of the apparatus implementing the cold ensemble exchange and dual-axis high-data-rate atom interferometer. (a) Front view: Two MOTs are loaded 36 mm apart. Cooling beams are shown in blue, probe beams in pink, and Raman beams in yellow. The trap is turned off, and the outer and inner cooling beams are blue and red detuned, respectively, which launches the ensembles towards each other. After the experiment, atoms are recaptured in the opposite trap to facilitate loading. (b) Side view: The design allows for four planes of optical access, enabling a compact apparatus. The vector **g** shows the direction of gravity, while **a** and Ω are the directions of acceleration and rotation measurement, respectively.
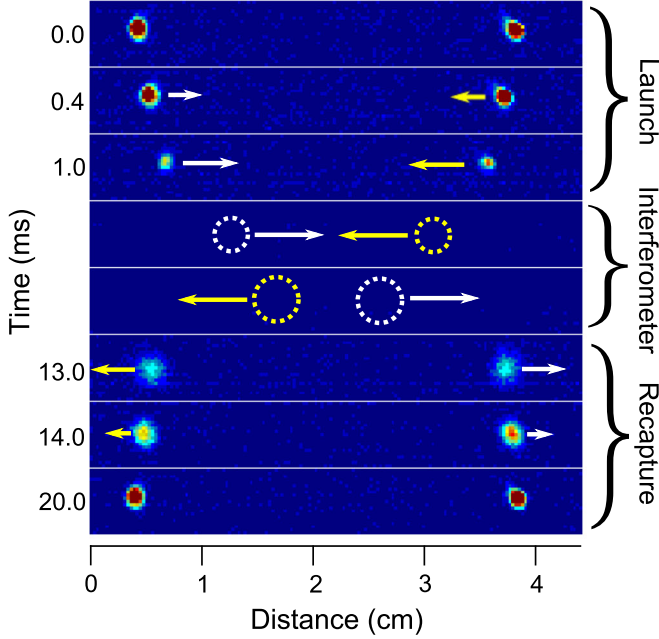
FIG. 2.   Frames from a movie [16] demonstrating the ensemble exchange with a cycle time of 20 ms. The ensembles are launched towards each other over 2 ms to a velocity of 2.5 m/s, with simultaneous sub-Doppler cooling. The interferometer takes place during their ballistic trajectory with an interrogation time $T \approx 4$ ms. Imaging beams are off during the interferometer to reduce photon scatter which would otherwise cause decoherence. Dashed circles represent the approximate positions of the ensembles during this stage. Atoms are then recaptured in the opposite trapping region, with additional atoms loaded from vapor for 7 ms. This cycle represents a high atom number, low-bandwidth cycle to optimize the image contrast. Images are taken with a Lumenera CCD camera (Lm075) using a 0.2-ms exposure.

III. RECAPTURE

We extend the well-known MOT loading equation [17] by including recapture between discrete shots of the experiment. We model the atom number for each shot n as a constant recapture fraction r_0, with a loss rate β and linear loading rate α. Furthermore, we assume a cycle time T_c, and a fraction of the cycle η reserved for recapture. The atom number may then be modeled as the sequential sum of atoms loaded from vapor, atoms recaptured, and atoms lost to background collisions. If we assume no density-induced losses, the atom number is given by the geometric sequence

$$N_{n+1} = \alpha \eta T_c + (r_0 - \beta T_c) N_n, \qquad (1)$$

with solution

$$N_n = \frac{\alpha \eta T_c}{1 - r}(1 - r^n), \qquad (2)$$

where $r = r_0 - \beta T_c$ is the net recapture efficiency. This assumes that the recapture time ηT_c is sufficiently larger

than the MOT relaxation time in order to recapture most of the available atoms. When the number of atoms which were not recaptured equals the number of atoms loaded from vapor, we achieve a steady-state atom number N_s given by

$$N_s = \lim_{n \to \infty} N_n = \frac{\alpha \eta T_c}{1 - r} = \frac{\alpha \eta T_c}{\beta T_c + (1 - r_0)}. \qquad (3)$$

For $r_0 < 1$ under low vapor pressure ($\beta T_c \ll 1 - r_0$), the loss rate is dominated by imperfect recapture. Thus, the steady-state atom number $N_s = \alpha \eta T_c/(1 - r_0)$ grows linearly in α. Under higher vapor pressure ($\beta T_c \gg 1 - r_0$), the loss rate is dominated by background vapor collisions, resulting in a steady-state atom number $N_s = \eta \alpha/\beta$. Assuming constant trap parameters, α and β are both proportional to vapor pressure. Therefore, similar to canonical MOT loading, the ratio α/β and, thus, the total atom number, are constant. Note that with $r_0 = 1$, $\eta = 1$, and in the limit of small T_c, N_n becomes the usual MOT loading equation [17],

$$N(t) = \frac{\alpha}{\beta}(1 - e^{-\beta t}). \qquad (4)$$

We test the efficacy of this model with two experiments. In the first, we explore the recapture dynamics of our apparatus, for a 20-ms cycle time. This is revealed by monitoring the atom number in the trap after the start of recapture until just prior to launch. This experiment is done in steady state, where the number of atoms lost in recapture is replenished by loading from vapor. Figure 3 demonstrates a large increase in atom number during the recapture process over a millisecond time scale. The large initial increase represents ensemble recapture from the previous shot of the experiment, with rN_s atoms loaded. To achieve steady state, an additional $\alpha \eta T_c$ atoms are loaded from vapor. By subtracting out the linear contribution and dividing by N_s, we calculate a recapture efficiency of $r = 85\%$. From the atom number $N_s = 7 \times 10^6$ and the size of the ensemble from Fig. 2, we calculate the peak atom density to be 8×10^8 atoms/cm³. This is well below the limit for density-induced losses [17], validating the assumption made [Eq. (1)].

As a second experiment, we measure the recapture efficiency by fitting Eq. (2) to the total atom number N_n over multiple shots of the experiment, while the process approaches steady state. Beginning with zero atoms, ensemble exchange will build the population to a steady state over 40 cycles. This is depicted in the inset of Fig. 4. Occasionally triggering the trapping coils on and off allows us to monitor the loading of atoms until steady state. Here, recapture efficiency is revealed by the number of cycles required to reach steady state.

The recapture efficiency and steady-state atom number are strongly affected by vapor pressure. Figure 4 depicts the observed and calculated recapture efficiency and
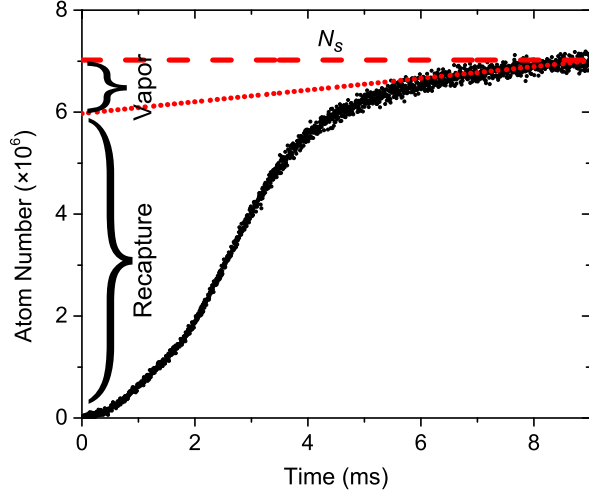
FIG. 3. Recapture process during steady-state ensemble exchange. Black dots show the atom number calculated from an avalanche photodiode (APD) signal as atoms are being recaptured and loaded into the trap. The red dashed line indicates the total steady-state atom number N_s, while the red dotted line is the vapor-loading rate contribution. Many atoms are loaded via recapture over a few milliseconds, followed by vapor loading to replenish the lost atoms. By subtracting out the vapor-loading contribution, we determine the net recapture efficiency to be $r = 85\%$. This includes losses due to background collisions during the cycle.

steady-state atom number over a range of vapor pressures, characterized by atom loss rate, β. We demonstrate a recapture efficiency ranging from 85% to 92%. The recapture efficiency decreases at higher vapor pressure due to an increased rate of collisions with background atoms during the ensemble's trajectory. However, the increased vapor-loading rate results in a net increase of steady-state atom number N_s, until an optimum of approximately 85% recapture efficiency is achieved at $\beta = 5$ 1/s. From this fit, we extrapolate the expected recapture efficiency at zero vapor pressure (no background losses) to 96%.

By minimizing the recapture time, we can increase the bandwidth of our experiment and achieve a higher sensitivity. One way to accomplish this is to decrease the trap time constant τ_{MOT} by employing a large magnetic-field gradient. However, this limits the maximum atom number in the trap. Accordingly, we employ a dynamic gradient of the quadrupole field. At the start of the recapture, a high field gradient lowers the time constant of the trap allowing for atoms to quickly relax into the trap. The field gradient is slowly ramped down over the remaining recapture time to increase the trap volume as atoms are loaded from vapor. For typical operating parameters, this results in an increase of 10% in steady-state atom number.

IV. INTERFEROMETER

We create the atom interferometer using stimulated Raman transitions. The Raman transitions arise from
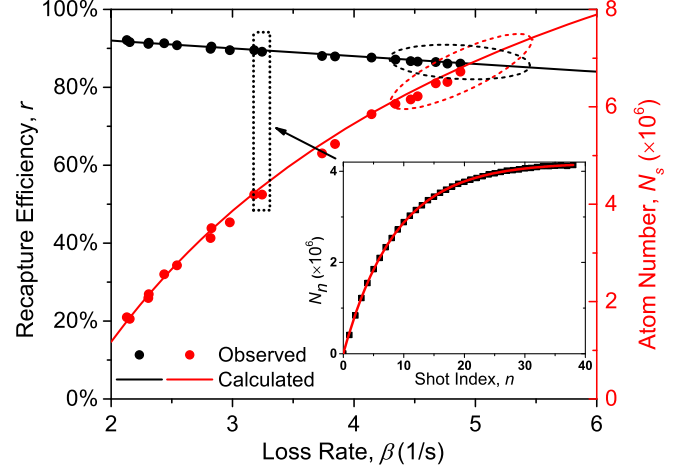

FIG. 4. Inset: Loading of the exchange MOT after starting with the traps off, at $\beta = 3.3$ 1/s. Each data point represents a single shot of the experiment. Fitting the data to Eq. (2) gives values for r and N_s at any given vapor pressure. Figure: Recapture efficiency r and steady-state atom number N_s as a function of loss rate β. Circles represent observed data during ensemble exchange. Solid lines are calculated from MOT loading parameters α and β, using the base recapture efficiency r_0 as a free parameter. The data show that sacrificing a moderate amount of recapture efficiency optimizes the atom number in the cycle due to a higher loading rate from vapor while the trap is active. The dashed circles show typical operating regimes, as well as the parameters for Fig. 3.

resonant pulses of light applied at three equispaced times during the ensemble's ballistic trajectory. The Raman beams are seeded from an external-cavity diode laser locked at 900 MHz red of the $|F = 2\rangle \rightarrow |F' = 3\rangle$ transition in ^{87}Rb. They are generated from the phase-coherent zero and first-order sidebands of a fiber-based electro-optic modulator operated at the hyperfine frequency. Following the modulator, the beams are amplified and shuttered by an acousto-optic modulator. Both sidebands are delivered to the apparatus via common optical paths to avoid unwanted relative phase noise. At the apparatus, we separate this light into three beams that are retroreflected from a shared 2-in.-diameter mirror that defines a common inertial reference. The positions of these three beams coincide with the positions of the ensembles at each of the three pulses in the $\pi/2$-π-$\pi/2$ interferometer pulse sequence. The polarization configuration is lin $\perp$ lin to suppress the Doppler-free transition.

The beams are delivered to the atoms at an angle of 10° from the orthogonal of the launch trajectory and are then retroreflected. This projects a component of the Raman beams along the velocity of the atoms, and the resulting Doppler shift of 1.1 MHz allows us to resolve both directions of the Raman wave vector $\mathbf{k}_e$ [18]. Selecting one of these wave vectors, we drive Doppler-sensitive Raman transitions between the hyperfine levels at three points along the trajectory of the atoms. Because of the

asymmetry of the velocity vector of the ensembles, a single detuning results in one interferometer with a vector of $+\mathbf{k}_e$ and another with $-\mathbf{k}_e$. Thus, the acceleration and rotation phase shifts are given by $\phi_- = \mathbf{k}_e \cdot \mathbf{a} T^2 = (\phi_a - \phi_b)/2$ and $\phi_+ = \mathbf{k}_e \cdot (2\mathbf{v} \times \mathbf{\Omega}) T^2 = (\phi_a + \phi_b)/2$, respectively.

In our apparatus, gravity is oriented $10°$ from the Raman beam axis, causing a chirp of the Raman transition resonance at a rate of 24.7 kHz/ms. However, due to the velocity vector asymmetry, this chirp is opposite for the two interferometers. This causes the resonances to separate in frequency space for the second and third pulses. Choosing an intermediate frequency allows both transitions to be resonant, although at a 20% lower efficiency for the final pulse. Raman beam arrangements that create identical $\mathbf{k}_e$ for both interferometers will eliminate this effect for a stationary device. However, a rotation rate of 5 rad/s in this latter case will cause the same effect.

A typical experiment cycle takes place in 16.66 ms, corresponding to a data rate of 60 Hz. Atoms are launched to 2.5 m/s and cooled over 1.5 ms to 35 μK. In addition to the repump beam, a π-polarized (D_1) optical pumping beam resonant with the $|F = 2\rangle \rightarrow |F' = 3\rangle$ transition transfers 92% of the atoms into the magnetically insensitive $|F = 2, m_F = 0\rangle$ state. A 1.5-G magnetic field parallel to the Raman beams defines a quantization axis. The atoms are then interrogated by the Raman beams with $T = 4.1$ ms at three points along their trajectory. The π-pulse length is 1.6 μs, allowing for the beams to address a wide velocity class of the atoms for each interferometer.

The population in $|F = 2\rangle$ and the total atom number are measured by fluorescence detection. The detection region

is smaller than the ensemble size as a means of velocity selection. Thus, only 30% of the total atoms in the ensemble exchange contribute to the interferometer signal, while the remaining 70% facilitate loading for the next shot. We collect 0.5% of the atoms' photon scatter from two 100-μs pulses. The first probe pulse measures the population in $|F = 2\rangle$. This is followed by both probe and repumping to measure the total population. The light is coupled into a 1-mm core multimode fiber that delivers it to an APD (Hamamatsu C5460-01). The collimators are aligned off axis by $2°$ to minimize cross-talk between the signals. From the ratio of the measured signals, we determine the probability to be in the excited state for each interferometer, from which the phase shifts ϕ_a and ϕ_b may be calculated. Given a fixed interrogation time, the sensitivity (per $\sqrt{\text{Hz}}$) is optimized with a 60-Hz ($T_c = 16.66$ ms) cycle. This restricts the recapture time to 6 ms and reduces the steady-state atom number to 4×10^6. Loading this many atoms in our apparatus from purely vapor will take 40 ms.

Figure 5 shows a sample fringe from the interferometer, with data taken at 60 Hz. We measure the phase noise of each interferometer to be $\delta\phi_a = \delta\phi_b = 22$ mrad/shot. The corresponding acceleration and rotation components of the phase noise are $\delta\phi_- = 19$ mrad/shot and $\delta\phi_+ = 11$ mrad/shot, respectively. The resulting acceleration and rotation sensitivities are 0.9 $\mu g/\sqrt{\text{Hz}}$ and 1.1 $(\mu\text{rad/s})/\sqrt{\text{Hz}}$ at 60 Hz. The rotation measurement benefits greatly from common-mode noise rejection of the vibrations of the retroreflecting mirror, with a phase noise approximately 2 times lower than the acceleration noise. It
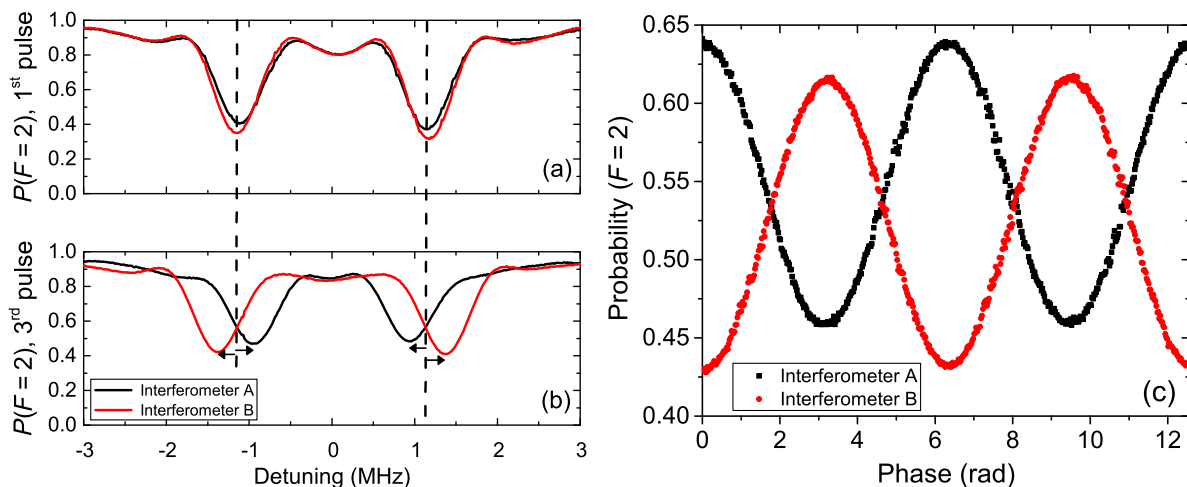

FIG. 5. (a) Transition probability as a function of the two-photon Raman detuning with respect to the hyperfine transition. The $10°$ projection of the Raman beam axis along the launch trajectory results in a Doppler shift, causing the resonance conditions of the two $\mathbf{k}_e$ vectors to be separated by 2.2 MHz. For a given choice of resonance, one interferometer is operated at $+\mathbf{k}_e$ while the other is at $-\mathbf{k}_e$. (b) Gravitational acceleration causes the resonance conditions to shift oppositely for each interferometer, resulting in the second and third pulses being driven off resonance. Technical limitations in Raman beam alignment give rise to an asymmetry in pulse efficiencies. (c) Sample fringes from the interferometer generated by scanning the electro-optical phase of the third pulse. The interferometer uses an interrogation time of $T = 4.1$ ms, and data are taken at 60 shots/s. We set a π phase difference between the interferometers by appropriate choice of T to suppress detection noise in favor of the rotation measurement.

is worth noting the potential performance of this approach under optimal conditions. If we assume a shot-noise limited signal with 4×10^6 atoms and 100% fringe contrast, with identical interrogation time and bandwidth, we calculate optimal sensitivities of $33 \, \mathrm{n} \, g/\sqrt{\mathrm{Hz}}$ and $70 \, (\mathrm{nrad/s})/\sqrt{\mathrm{Hz}}$.

The noise in our system derives from reduced fringe contrast and detection noise. The size of the ensemble relative to the size of the Raman beams causes Rabi-frequency inhomogeneities, which reduce the overall population transfer efficiency. Additionally, the width of the Raman transition in frequency space must be large enough to address the Doppler shifts from the thermal velocity distribution of the atoms. These effects result in a π-pulse efficiency of 55% for the first pulse. It is likely that a combination of an expanding position distribution and the 24.7-kHz/ms gravity-induced Doppler shift reduces the π-pulse efficiency of the third pulse to 35%, resulting in a fringe contrast of 20%. Accounting for the fraction of the ensemble imaged and the fringe contrast, 1×10^6 atoms contribute to the measured noise while 2×10^5 atoms contribute to the signal. From this, we expect a noninertial phase noise of 5 mrad per interferometer, corresponding to $\delta\phi_{\pm} = 3.5$ mrad. Electronic noise, background scatter, and photon shot noise are negligible. Thus, we attribute the noise in our system to stability of the inertial reference, and frequency and intensity noise of the probe.

Decoupling the phase shifts of acceleration and rotation is optimized when $\mathbf{v}_a = -\mathbf{v}_b$. Otherwise, a systematic error results from cross-coupling of the rotation phase shift into the acceleration phase shift, requiring calibration. In our apparatus, we estimate an upper bound of 5% speed difference between the ensembles and an angular deviation of the velocity vectors from antiparallel of 30 mrad. From this, we calculate a maximum cross-coupling of 3% of the Earth-rate phase shift into the acceleration phase shift, which falls below the current resolution. The effect of fractional velocity noise $|\boldsymbol{\delta v}|/|\mathbf{v}| = 10^{-4}$ per shot is negligible.

The most direct route towards enhancing the sensitivity is by improving fringe contrast. It is possible to implement independent detunings for the third pulse by adding a second independently controllable Raman laser. Additionally, the increased Raman power enables one to reduce Rabi-frequency inhomogeneity by increasing Raman beam waist, further improving pulse efficiency. Pulse efficiency can also be improved by using composite pulses [5,19,20].

V. DYNAMICS

Operating the interferometer in a dynamic environment beyond benign laboratory conditions of 1 g and 100 μrad/s demands robustness. Additionally, the apparatus must be able to handle large changes in acceleration (jerk) and rotation (angular acceleration). We motivate further research in this vein by exploring the more dynamic

features of our approach compared to conventional atom interferometers.

Gravitational acceleration in conventional atom interferometers with $T \approx 100$ ms causes an atomic ensemble to traverse tens of centimeters. Thus, they are designed accounting for a fixed orientation of gravity. Under an arbitrary orientation of gravity, the apparatus will not function due to the ensemble's deflection. A short interrogation time minimizes the deflection and allows for our interferometer to operate in any orientation. To demonstrate this, we rotate the apparatus over a range of angles in the plane defined by $\mathbf{v}$ and $\mathbf{k}_e$. This changes the projection of gravity on these vectors. As shown in Fig. 6, the fringe contrast and the atom number remain unchanged to within the measurement uncertainty over a range of angles. The apparatus is designed to exhibit a certain detection and recapture volume. Under a reversal of gravity orientation, the ensemble does not violate these boundaries.

To estimate the acceleration and rotation rate the ensemble exchange can endure, we measure the recapture efficiency as a function of ensemble distance from the trap center at the onset of recapture. By triggering the trap at different delay times following the launch, we simulate recapture at different locations along the launch vector, $\hat{\mathbf{x}}$ (Fig. 7). While the launch velocity direction causes an asymmetry where early activation still allows the atoms to relax into the trap, results for a delayed activation should mirror deflections along the $\hat{\mathbf{y}}$ and $\hat{\mathbf{z}}$ axes. We empirically measure the recapture radius along $\hat{\mathbf{x}}$ to be 5 mm, where the recapture efficiency falls below 50%. Dynamic conditions as large as 10 g of acceleration and 20 rad/s of rotation will be necessary to replicate this level of excursion.
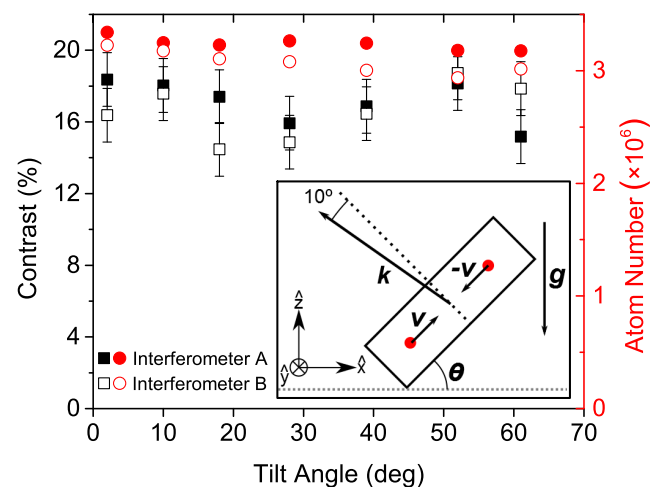

FIG. 6.   Immunity of the atom interferometer to a range of tilt. The tilt direction corresponds to θ_y, thus, changing the projection of gravity on the Raman beam axis, as well as the launch axis. Error bars represent the long-term drift seen in the apparatus over 1 h when the interferometer is flat on the table. The fringe contrast and steady-state atom number are largely unaffected by the orientation.
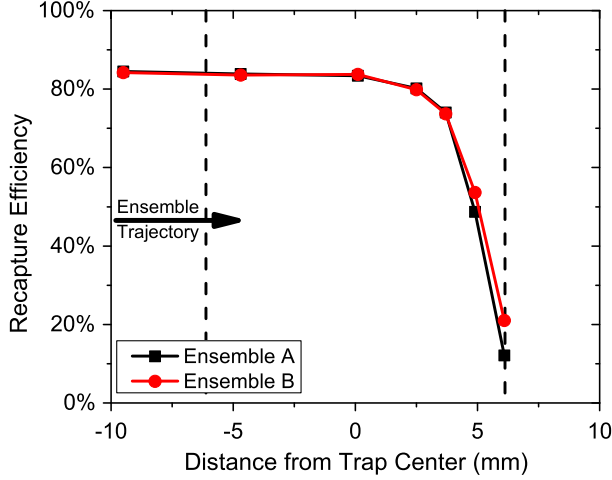
FIG. 7. Recapture efficiency over a range of ensemble positions relative to the trap center, at the onset of ballistic recapture. Dashed lines represent the $1/e^2$ diameter of the trapping volume. For early onset (negative position), the ensemble's momentum still carries it into the trap. Recapture is still efficient over a large fraction of the trap volume.

Although the ensemble exchange tolerates a large range of inertial conditions, successfully tracking the inertial signals requires that jerk and angular acceleration be limited to an amount equivalent to a $\pi/2$ interferometer phase shift over one interferometer cycle. This corresponds to a jerk of $|\mathbf{j}| = \pi/(2|\mathbf{k}_e|T^2 T_c)$, and an angular acceleration of $|\boldsymbol{\alpha}| = \pi/(4|\mathbf{k}_e||\mathbf{v}|T^2 T_c)$. Exceeding these rates can be enabled by using complementary auxiliary sensors.

An alternative rotation rate limit arises from phase gradients in the ensemble due to the thermal velocity distribution, leading to loss of contrast. Each atom derives an independent rotation phase shift due to its thermal velocity coupled with the rotation rate. For a given characteristic velocity width σ_v, when the rotation rate exceeds the condition $|\Omega| > \pi/(2|\mathbf{k}_e|\sigma_v T^2)$, large inhomogeneous dephasing occurs [13]. Given a rotation of magnitude Ω at an angle of θ from $\hat{\mathbf{k}}_e$, and an ensemble temperature of $\mathcal{T}$, the decay of the fringe contrast χ is given by

$$\chi(\Omega) = \exp\left(\frac{-\Omega^2}{2\sigma^2}\right),$$

$$\sigma = \frac{1}{2}\sqrt{\frac{m}{k_B \mathcal{T}}} \frac{1}{|\mathbf{k}_e|T^2 \sin(\theta)}, \qquad (5)$$

where m is the mass of ^{87}Rb, and k_B is the Boltzmann constant.

We demonstrate this effect by placing the apparatus on a 22-cm-diameter rotation platform located outside of the magnetic shielding. The experiment is configured to rotate about $\pm\hat{\mathbf{g}}$ in Fig. 1, or $\theta = 10°$. The angular position of the platform is recorded via a rotary encoder. Figure 8 shows
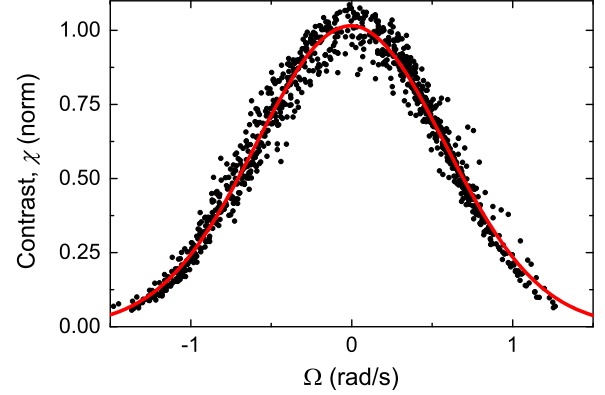

FIG. 8. Contrast loss under high rotation rate. The black points are the observed fringe contrast as the apparatus is rotated in the $\pm\hat{\mathbf{g}}$ direction, up to ± 1.5 rad/s. The red line is a Gaussian fit, with a width of $\sigma = 0.60(1)$ rad/s.

measurements of the fringe contrast while rotating the apparatus in the $\pm\hat{\mathbf{g}}$ direction up to ± 1.5 rad/s. We observe a minimal change in atom number of a couple percent at 1 rad/s for a duration of 1 s. At sustained rates where the ensemble is allowed to hit steady state, we expect the atom number to be slightly less. As expected, the contrast loss is Gaussian with respect to the rotation rate Ω. The characteristic width of the distribution is $\sigma = 0.60(1)$ rad/s, which corresponds to a temperature of 36 μK. This is in agreement with independent temperature measurements. The most severe limit will arise if we rotate the apparatus perpendicular to $\hat{\mathbf{k}}_e$, which will cause the contrast to vanish $\sin(90°)/\sin(10°) \approx 6$ times faster. This limit can be extended by cooling to lower temperature or by placing the apparatus on gimbals. Although the ensemble contrast is diminished, the individual atoms still maintain phase coherence and inertial purity. If the ensemble meets the condition $2T\sigma_v \gg \sigma_{x_0}$, where σ_{x_0} is the initial characteristic position width, the position of each atom during detection corresponds strongly with its velocity. Then, the inertial information for each velocity class may be retrieved with a sufficiently well-resolved detector [21].

VI. CONCLUSION

We demonstrate a high-data-rate atom interferometer capable of simultaneous acceleration and rotation measurements at 60 Hz, with sensitivities suitable for a wide application space. The system makes use of the ensemble exchange technique to launch and recapture atoms at a high data rate, orders of magnitude higher than typical LPAI systems. We model the atom number during ensemble exchange assuming a fixed recapture fraction and validate the model with experiments. Additionally, we characterize our interferometer and estimate the potential performance of our design. We show immunity of recapture efficiency and interferometer contrast over a range of acceleration and rotation values.

Our ensemble exchange method enables a path towards a compact atomic inertial measurement unit. Further work is needed to miniaturize the remainder of the system and achieve the ultimate sensitivity. We consider a device with sensitivities of approximately $10\,\mathrm{n}\,g/\sqrt{\mathrm{Hz}}$ and $10\,(\mathrm{nrad/s})/\sqrt{\mathrm{Hz}}$, and robust up to approximately $10\,g$ and $10\,\mathrm{rad/s}$ to be feasible in an engineered package that is significantly smaller than our apparatus. Through careful study of the apparatus' dynamics, we may model the sensor response in various scenarios and enable a fielded device.

ACKNOWLEDGMENTS

[1] F. Riehle, Th. Kisters, A. Witte, J. Helmcke, and Ch. J. Bordé, Optical Ramsey spectroscopy in a rotating frame: Sagnac effect in a matter-wave interferometer, Phys. Rev. Lett. **67,** 177 (1991).

[2] Mark Kasevich and Steven Chu, Atomic interferometry using stimulated Raman transitions, Phys. Rev. Lett. **67,** 181 (1991).

[3] Susannah M. Dickerson, Jason M. Hogan, Alex Sugarbaker, David M. S. Johnson, and Mark A. Kasevich, Multiaxis inertial sensing with long-time point source atom interferometry, Phys. Rev. Lett. **111,** 083001 (2013).

[4] Q. Bodart, S. Merlet, N. Malossi, F. Pereira Dos Santos, P. Bouyer, and A. Landragin, A cold atom pyramidal gravimeter with a single laser beam, Appl. Phys. Lett. **96,** 134101 (2010).

[5] J. M. McGuirk, G. T. Foster, J. B. Fixler, M. J. Snadden, and M. A. Kasevich, Sensitive absolute-gravity gradiometry using atom interferometry, Phys. Rev. A **65,** 033608 (2002).

[6] B. Canuel, F. Leduc, D. Holleville, A. Gauguet, J. Fils, A. Virdis, A. Clairon, N. Dimarcq, Ch. J. Bordé, A. Landragin,

and P. Bouyer, Six-axis inertial sensor using cold-atom interferometry, Phys. Rev. Lett. **97,** 010402 (2006).

[7] Saijun Wu, Edward Su, and Mara Prentiss, Demonstration of an area-enclosing guided-atom interferometer for rotation sensing, Phys. Rev. Lett. **99,** 173201 (2007).

[8] L. P. Parazzoli, A. M. Hankin, and G. W. Biedermann, Observation of free-space single-atom matter wave interference, Phys. Rev. Lett. **109,** 230401 (2012).

[9] Yannick Bidel, Olivier Carraz, Rene Charrire, Malo Cadoret, Nassim Zahzam, and Alexandre Bresson, Compact cold atom gravimeter for field applications, Appl. Phys. Lett. **102,** 144107 (2013).

[10] T. Muller, M. Gilowski, M. Zaiser, P. Berg, Ch. Schubert, T. Wendrich, W. Ertmer, and E. M. Rasel, A compact dual atom interferometer gyroscope based on laser-cooled rubidium, Eur. Phys. J. D **53,** 273 (2009).

[11] Hayden J. McGuinness, Akash V. Rakholia, and Grant W. Biedermann, High data-rate atom interferometer for measuring acceleration, Appl. Phys. Lett. **100,** 011106 (2012).

[12] *Atom Interferometry*, edited by P. R. Berman (Academic Press, New York, 1997).

[13] T. L. Gustavson, A. Landragin, and M. A. Kasevich, Rotation sensing with a dual atom-interferometer Sagnac gyroscope, Classical Quantum Gravity **17,** 2385 (2000).

[14] David L. Butts, Joseph M. Kinast, Brian P. Timmons, and Richard E. Stoner, Light pulse atom interferometry at short interrogation times, J. Opt. Soc. Am. B **28,** 416 (2011).

[15] H. Metcalf and P. van der Straten, *Laser Cooling and Trapping* (Springer, New York, 1999).

[16] See Supplemental Material at http://link.aps.org/supplemental/10.1103/PhysRevApplied.2.054012 for a video demonstrating the cold ensemble exchange.

[17] A. M. Steane, M. Chowdhury, and C. J. Foot, Radiation force in the magneto-optical trap, J. Opt. Soc. Am. B **9,** 2142 (1992).

[18] J. K. Stockton, K. Takase, and M. A. Kasevich, Absolute geodetic rotation measurement using atom interferometry, Phys. Rev. Lett. **107,** 133001 (2011).

[19] David L. Butts, Krish Kotru, Joseph M. Kinast, Antonije M. Radojevic, Brian P. Timmons, and Richard E. Stoner, Efficient broadband raman pulses for large-area atom interferometry, J. Opt. Soc. Am. B **30,** 922 (2013).

[20] Alexander Dunning, Rachel Gregory, James Bateman, Nathan Cooper, Matthew Himsworth, Jonathan A. Jones, and Tim Freegarde, Composite pulses for interferometry in a thermal cold atom cloud, Phys. Rev. A **90,** 033608 (2014).

[21] Alex Sugarbaker, Susannah M. Dickerson, Jason M. Hogan, David M. S. Johnson, and Mark A. Kasevich, Enhanced atom interferometer readout through the application of phase shear, Phys. Rev. Lett. **111,** 113002 (2013).